nature energy

SUPPLEMENTARY INFORMATION
https://doi.org/10.1038/s41560-018-0243-8

In the format provided by the authors and unedited.

Efficient thermal management of Li-ion batteries with a passive interfacial thermal regulator based on a shape memory alloy

Menglong Hao [1], Jian Li [1,2], Saehong Park [3], Scott Moura [3] and Chris Dames [1,4]*

[1]Department of Mechanical Engineering, University of California, Berkeley, CA, USA. [2]Key Laboratory of Energy Thermal Conversion and Control of Ministry of Education, School of Energy and Environment, Southeast University, Nanjing, China. [3]Energy, Controls, and Applications Lab, Department of Civil and Environmental Engineering, University of California, Berkeley, CA, USA. [4]Materials Sciences Division, LBNL, Berkeley, CA, USA.
*e-mail: cdames@berkeley.edu

Supplementary Information

Supplementary Note 1

Kinematics optimization discussion

Optimizing the performance of this thermal regulator requires tradeoffs among multiple competing objectives, some of which can be understood graphically from Fig. 2(b). From the mechanical perspective, we would like to maximize both $\Delta\varepsilon$ (for a bigger gap in the OFF state and therefore lower G_{off}) and $\sigma_{contact}$ (for a higher interfacial contact P and thus higher G_{on}). Figure 2(b) shows that $\Delta\varepsilon$ can be increased by shifting the zero-gap line (the vertical line connecting "Int." and "ON") further to the left, which can be done by using a longer wire. However, Fig. 2(b) also shows that in doing so $\sigma_{contact}$ will unfortunately decrease, thereby reducing P (which is $\sigma_{contact}$ scaled by the ratio $\pi d^2/W^2$,where d is the wire diameter). Similarly, if the bias spring response line is shifted upward (by increasing the pre-strain in the bias springs), the device would have a larger $\Delta\varepsilon$ but lower $\sigma_{contact}$. The wire diameter d also has competing effects: thicker wire will result in a larger P_{on} (favorable for G_{on}) but increase the heat flow by conduction through the wire (an unfavorable parasitic for G_{off}). A wire diameter of 254 μm (0.010") was found by experimentation to yield the best results and therefore chosen for our main results. The thermal interface material (TIM) is another key factor in obtaining a high G_{on}, especially considering that the available contact pressure is not high (~50 kPa). The cyclic stability of the TIM must be taken into account as well. A BN-filled solid silicone film (Laird TPLI210) was selected over common thermal grease as the latter suffers from durability issues such as pump-out [1].

Supplementary Note 2

Model prediction of thermal conductance from reference bar experiments

A simple one-dimensional heat transfer model is used to estimate G_{on} and G_{off} from the reference bar experiment. For the "OFF" state, there is no direct thermal conductance between the two surfaces. However, thermal radiation, heat conduction through the SMA wire, and heat convection (if not in vacuum) all contribute to the thermal conductance in parallel. The two opposing surfaces are BN filled silicone elastomer (TIM) and Cu-coated polished stainless steel, with emissivities of ε_1≈0.75 and ε_2≈0.1 (measured using Fourier-transform infrared spectroscopy (FTIR)), respectively. Therefore, the radiation heat flux can be calculated as

$$q_{rad} = \frac{\sigma(T_1^4 - T_2^4)}{\frac{1-\varepsilon_1}{\varepsilon_1} + 1 + \frac{1-\varepsilon_2}{\varepsilon_2}}, \qquad \text{(Suppl. Eq. 1)}$$

with σ being the Stefan-Boltzmann constant (5.67×10^{-8} W/m^2K^4) and T_1 and T_2 being the surface temperatures in Kelvin. For the "OFF" state shown on the left side of Fig. 3b, T_1 and T_2 are around 48°C and 22°C, respectively. The radiation contribution to G_{on} is then

$$G_{rad} = \frac{q_{rad}}{T_1 - T_2} \approx 0.64\, W/m^2K. \quad \text{(Suppl. Eq. 2)}$$

The contribution of conduction through the SMA wires to G_{on} is more difficult to estimate because the structure of the relevant pathway is complex. However, its upper bound can be calculated by ignoring thermal resistance between the wire and the bars,

$$G_{cond}\ (upper\ bound) = \frac{\kappa_{wire}}{L} \cdot \frac{4 \cdot A_{wire}}{A_{bar}} \approx 0.61\, W/m^2K, \quad \text{(Suppl. Eq. 3)}$$

with $L\approx0.7$ mm being the exposed length of SMA wire connecting the two bars and A being the cross-sectional area. Because of the contact resistance and low thermal conductivity of PEEK (0.29 W/m-K), we estimate that the true G_{cond} is lower than this upper bound by up to a factor of 2. Therefore, in vacuum G_{on} is between 0.94 and 1.25 W/m^2K.

As for the "ON" state, the thermal transport is dominated by direct heat conductance between the surfaces through the TIM. Precise estimation of this conductance requires the full mechanical characteristics of the SMA wire as well as the pressure-dependent performance of the TIM, both of which are not given by the respective vendors. However, based on the information available, we still derived a range of expected G_{on}. The exact mechanical property of Nitinol depends on the heat treatment, but a typical stress-strain relation can be found in Ref. [2]. The useful actuation stress $\sigma_{contact}$ (determined by the balance of wire restoration force and bias spring force, see Fig. 2(b)) is around 100-200 MPa. The contact pressure between the two surfaces should be

$$P = \sigma_{contact} \cdot \frac{4 \cdot A_{wire}}{A_{bar}} \cdot cos\theta, \quad \text{(Suppl. Eq. 4)}$$

with θ being the angle between the z axis and the portion of the wire connecting the two bar. The area ratio $\frac{4 \cdot A_{wire}}{A_{bar}}$ is approximately 1:2020 and θ is roughly 45°. Therefore, the contact pressure is expected to be in the 35-75 kPa range. The TIM used in this study is a Laird TPLI210. The thermal conductance is stated by the vendor to be approximately 9,700 W/m^2K at 138 kPa. In-house measurements in vacuum environment using the same stainless steel bars as Fig. 3 of the main text gave a thermal conductance of around 4,050 W/m^2K for this TIM at a contact pressure of 100 kPa, which we take as the upper bound of G_{on}. Considering that the actual pressure is much lower (down to 35 kPa) and the fact that TIMs typically have a sublinear dependence of G on P, we estimate G_{on} to be in the range of 2000-3000 W/m^2K. Hence, this model predicts that a switch ratio of at least

$$SR_{vac.} = \frac{G_{on}}{G_{off}} > \frac{2000}{1.25} \approx 1600 \quad \text{(Suppl. Eq. 5)}$$

can be achieved in vacuum.

In an ambient air environment, however, the switch ratio will be much lower. Now G_{off} is dominated by parasitic heat conduction through air,

$$G_{off} = \frac{\kappa_{air}}{D} = \frac{25\ mW/m{-}K}{0.5\ mm} = 50\,\frac{W}{m^2K}. \qquad \text{(Suppl. Eq. 6)}$$

Ignoring any slight increase in G_{on} due to air helping the bar-TIM contacts, the estimated switch ratio is now

$$SR_{air} = \frac{G_{on}}{G_{off}} > \frac{2000}{50} \approx 40. \qquad \text{(Suppl. Eq. 7)}$$

Supplementary Note 3

Data evaluation for reference bar experiments

The steady-state reference bar method assumes constant heat flux along the bars and through the interface. However, this is not strictly true considering losses by convection and thermal radiation from the side walls of the reference bars. Convection is negligible in our high vacuum environment (~10^{-6} torr), but the radiation losses are detectable, manifested as a slight deviation between the temperature gradients of upper and lower bars (Supplementary Figure 1). We now analyze this “radiation fin.” The bar sidewalls exchange radiation with the walls of the large vacuum chamber, which can be treated as a black body at $T_{chamber}$=21°C. The heat transfer governing equation for the stainless steel bars taking into account this thermal radiation is

$$\frac{\partial}{\partial z}\left(\kappa A\,\frac{\partial T}{\partial z}\right) = q_{rad.} = 4W\varepsilon\sigma\left(T^4 - T^4_{chamber}\right), \qquad \text{(Suppl. Eq. 8)}$$

where κ is the thermal conductivity of type-304 stainless steel (treated as a constant here since the involved temperature range is not very large) [3], A=400 mm^2 is the cross-sectional area of the bars, T(z) the bar temperature at an axial location z, ε the bar emissivity, and $4W$=80 mm the perimeter of the bars. Based on this model, the temperature profile can be precisely captured by numerically fitting 4 parameters to the 8 T(z) data points: G, ε, and the temperature and heat flux at the interface (method previously reported [4]). As shown in Supplementary Figure 1 (lower panel), the agreement with experimental data is better than that using the simple linear model ignoring radiation (upper panel). However, the difference in the thermal conductance obtained by these two methods is small, for example, around 5% if we use the temperature gradient on the lower bar in the linear model (Eq. (3)&(4) of main text). Radiation heat flux linearly scales with the 4th power of absolute temperature, so the radiation loss from the lower bar is weaker and thus the heat flux obtained from the lower bar is closer to the true heat flux through the interface. For model simplicity and avoidance of free fitting parameters, we elect to evaluate G using the simple linear method and obtain heat flux from the lower bar.

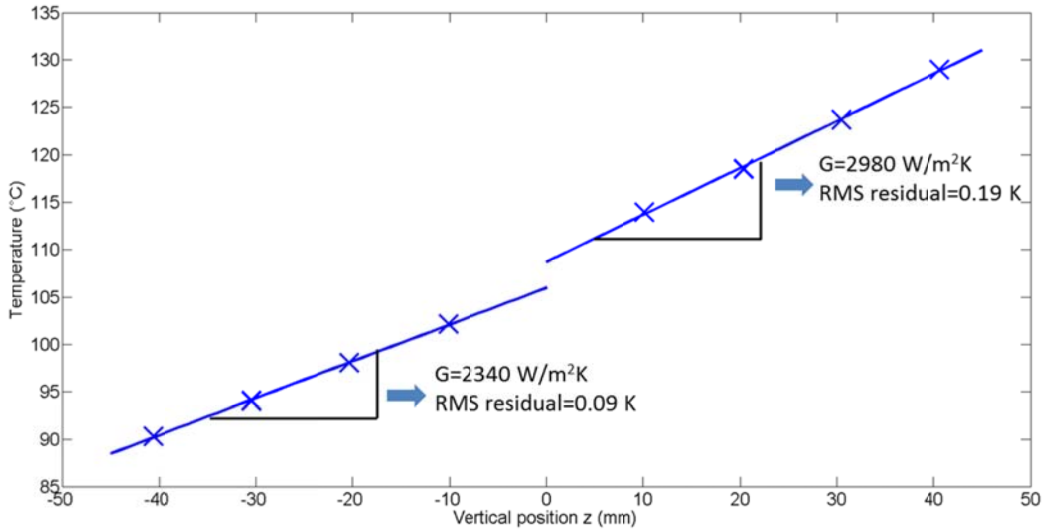

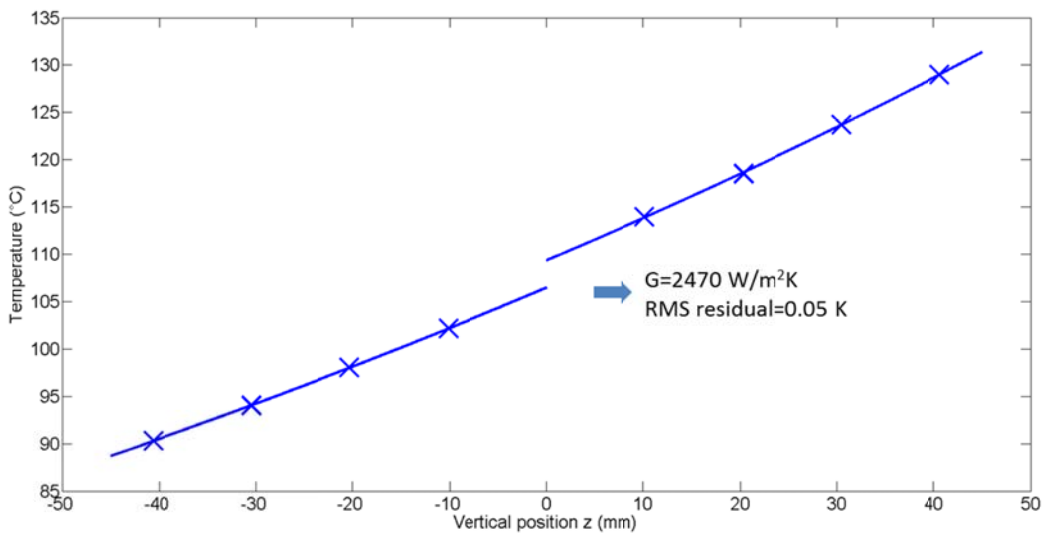

Supplementary Figure 1. Upper panel: linear fitting of the temperature profile for an "ON" state. Using upper and lower bar to calculate heat flux from Eq. (2) of main text yields thermal conductance of 2980 and 2340 W/m^{2}K, respectively. Lower panel: nonlinear numerical fitting of the same dataset considering radiation. The emissivity is fitted to be 0.25, which agrees with FTIR results. This is a more accurate estimation of the thermal conductance as validated by the lower RMS residual value. This fitting result is 5% higher than that obtained from lower bar using the linear method.

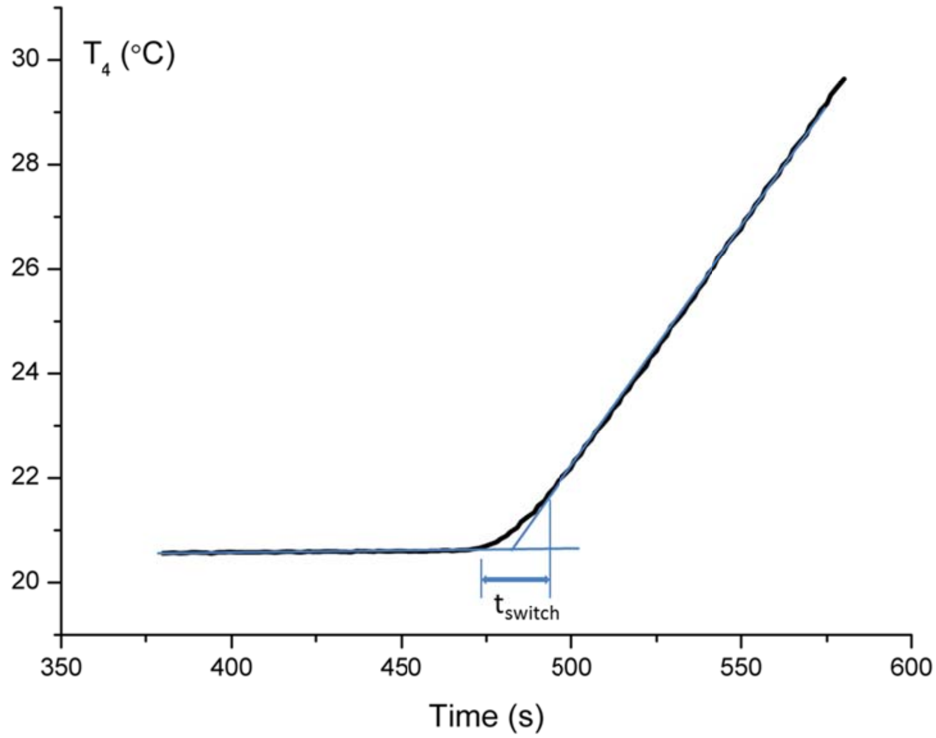

Supplementary Figure 2. The magnified transient temperature curve of T_4 (uppermost thermocouple on the lower bar) during the switch-on process shown in Fig. 3(e) of the main text. Notably, the transition from a flat temperature (weak thermal transport across the interface, “OFF”) to a rapid temperature rise (strong thermal transport across the interface, “ON”) occurs in roughly 10-20 seconds. This transition time estimation is in fact an upper bound considering the thermal diffusion time over the 10 mm of SS from the surface to T_4 location.

Supplementary Note 4

TRIP and thermal regulator cyclability

Cyclability and durability are critical requirements for mainstream adoption of thermal regulators, especially for battery applications. Our results show that carefully pre-conditioning the SMA allows the present thermal regulator to be robust and durable over repeated cycles (Fig. 3 (f)). Using unconditioned SMA wire as-received results in G_{on} decreasing by more than 60% after merely 3 cycles as shown in Fig. 3(f) (open points), caused by the well-known transformation-induced plasticity (TRIP) effect [5]. When SMA goes through thermally induced phase transformation under continuous load, it recovers most, but not all, of the pseudoelastic strain, leaving a small amount of permanent elongation. Therefore, the SMA wire’s relaxed length becomes longer and the contact pressure becomes lower from cycle to cycle. Fortunately, this TRIP effect is stronger in initial cycles and finally saturates after 100s or 1000s of cycles [6], and thus is mitigatable if the SMA wire is repeatedly cycled prior to use in the thermal regulator. To accelerate the time-consuming training process, a separate apparatus is used to train the wire at a higher stress (~350 MPa) than ultimately required in the thermal regulator (~200 MPa). With 200 cycles of this pre-treatment of the SMA wire, the thermal switch has shown high switch ratio (average 2020:1 ±130 (stdev)) with good cyclic stability in the 10 cycles we have tested in vacuum (linear regression of the data in Fig.3f even suggests a slightly increasing trend in switch ratio) as well as in the 1000 switch cycles in air.

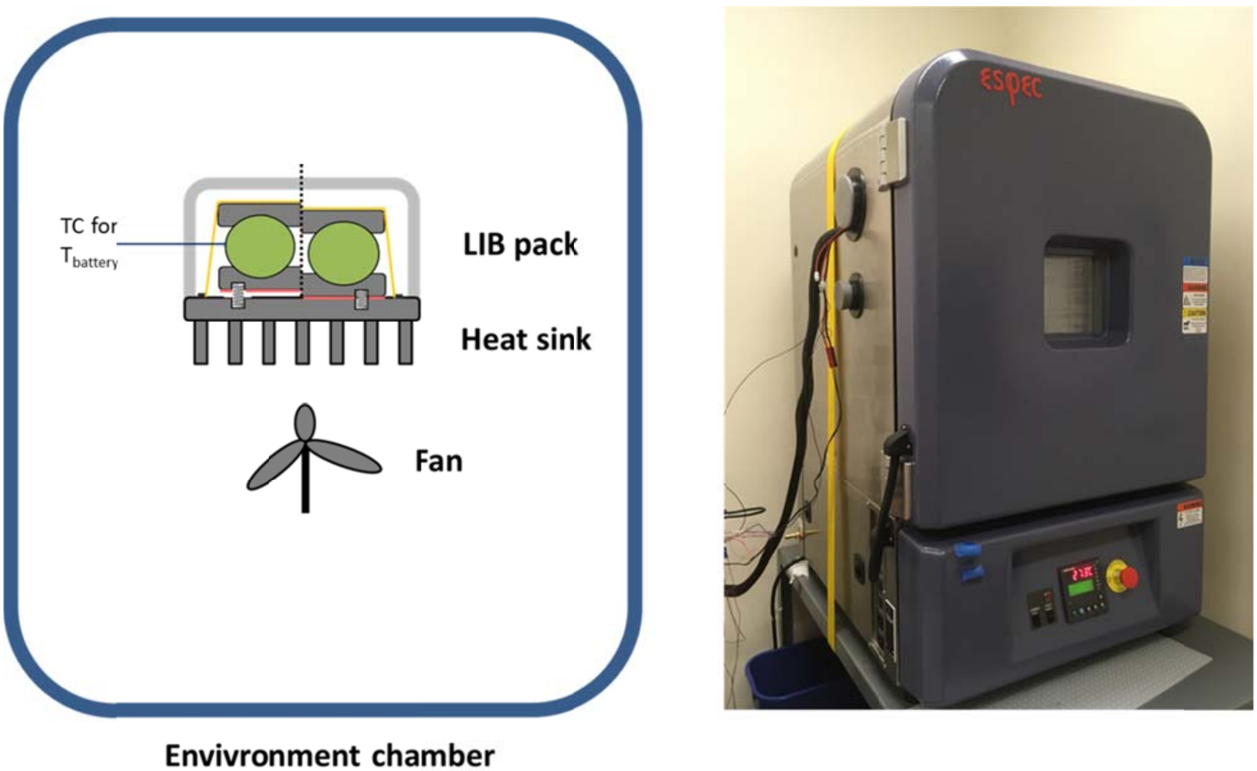

Supplementary Figure 3. Left: schematic of the test setup for thermally regulated battery pack, used for the results of Fig. 4 of the main text. The battery pack assembly, heat sink, and fan are all in an environmental chamber, which holds the temperature to set values within ±1°C. Right: photo of the environmental chamber used for this study (ESPEC BTL-433).

Supplementary Note 5

The effect of parallel and series thermal resistances

A simple thermal circuit model is presented here to analyze the effects of parallel and series thermal resistances in the battery experiment.

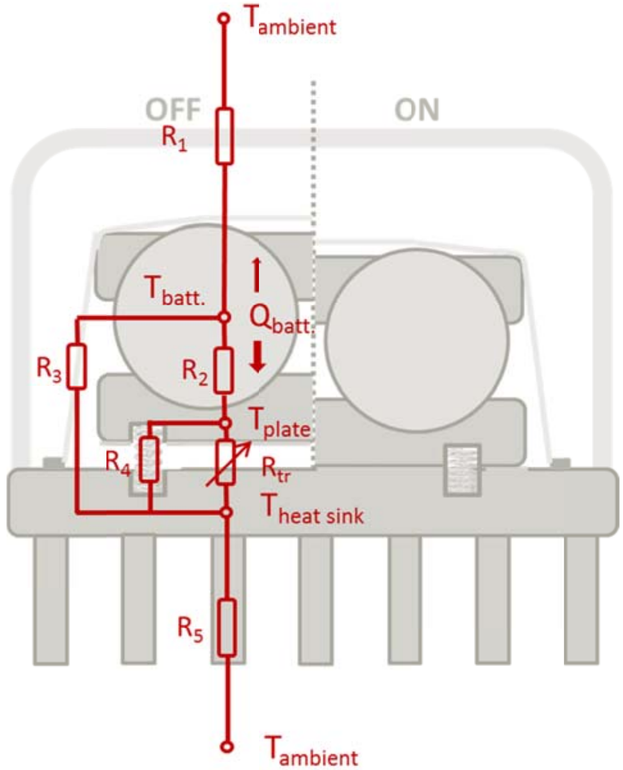

Supplementary Figure 4. A simple thermal circuit model showing the parallel thermal pathways and series thermal resistors.

In ambient air, we have estimated that closing and opening a 1 mm thermal regulator gap (R_{tr}) leads to a switch ratio (SR) of 40, a best case value. Free convection to ambient air (R_1), although largely suppressed by the aerogel blanket, is a parallel thermal pathway which reduces the system-level R_{off}. Other parallel thermal pathways include heat conduction through the SMA wire (R_3) and the springs (R_4), which are much less conducting than R_1 and therefore neglected. Undesirable series resistances include the battery-plate thermal interface resistance (R_2) and heat sink-ambient air convective thermal resistance (R_5), because they increase the system level R_{on}. Taking into account these parallel and series resistances, the estimated SR of the system is reduced to 16. For future implementations, there are some measures that can potentially increase the system SR by mitigating the effects of the parallel pathways and series resistances. In a large battery pack where many such modules are closely packed, adjacent pairs of modules will see symmetrical boundary conditions, so that the free convection (R_1) parallel pathway could be almost eliminated. If liquid cooling is adopted (as in Chevy Volt and Tesla EVs), R_5 could be also greatly reduced. Taking R_1 as infinitely large and R_5 reduced by 80%, the estimated system SR would increase to 27.

Supplementary Table 1. Estimated values for various thermal resistors in the module. All thermal resistances are normalized to the switched interface contact area S_{int} (i.e., the interface with the TIM, 0.003 m^2).

Thermal resistor	Thermal resistance (mm^2K/W)	Assumptions
R_1	150,000	Module-to-aerogel natural convection: h=10 W/m^2K Module surface area: S_m=0.006 m^2 Aerogel surface area: S_a=0.007 m^2 Aerogel thermal conductivity: k_a=0.017 W/m-K [7] Aerogel thickness: t_a=4 mm $R_1 \approx \frac{1}{h} \cdot \frac{S_{int}}{S_m} + \frac{t_a}{k_a} \cdot \frac{S_{int}}{S_a}$ The aerogel-to-ambient resistance is comparatively much lower due to a forced convection boundary condition (air is circulated in the chamber to ensure temperature uniformity) and therefore neglected in this analysis.
R_2	400	R_2 is estimated experimentally by scaling $R_{tr(on)}$ using additional thermocouples on the holder plate and heat sink, using the following relation in the “ON” state, $R_2 = \left(\frac{T_{batt.} - T_{plate}}{T_{plate} - T_{heat\,sink}}\right) \cdot R_{tr(on)}$. This value is consistent with an estimate using the properties of the silicone grease used for this interface, using the following assumptions: Contact area of this interface is similar to S_{int}. Grease thermal conductivity: k_g=3 W/m-K [8] Grease bond line thickness: t_g≈120 µm $R_2 = \frac{t_g}{k_g}$
R_3	>10^7	SMA thermal conductivity: k_{SMA}≈10 W/m-K [9] SMA length (connecting module with heat sink): L_{SMA}≈0.025m SMA cross-section area (single wire): $S_{SMA} = \pi \cdot (127\ \mu m)^2$. 4 wire connections in parallel. $R_3 = \frac{L_{SMA}}{k_{SMA}} \cdot \frac{S_{int}}{4 \cdot S_{SMA}}$
R_4	>10^6	Spring thermal conductivity: k_{Spring}≈16 W/m-K [3] Spring length: L_{Spring}≈0.05m Cross-section area of single spring: $S_{Spring} = \pi \cdot (500\ \mu m)^2$ 5 springs in parallel. $R_4 = \frac{L_{Spring}}{k_{Spring}} \cdot \frac{S_{int}}{5 \cdot S_{spring}}$
R_5	600	R_5 is estimated experimentally by scaling $R_{tr(on)}$ using additional thermocouples on the holder plate and heat sink, using the following relation in the “ON” state, $R_5 = \left(\frac{T_{heat\,sink} - T_{ambient}}{T_{plate} - T_{heat\,sink}}\right) \cdot R_{tr(on)}$.
$R_{tr(on)}$	1,000	Estimated as twice the ON state resistance in the reference bar experiment due to larger contact area and thus lower contact pressure
$R_{tr(off)}$	40,000	Air thermal conductivity: k_{air}≈0.025 W/m-K Gap size: L_{gap}≈1 mm $R_{tr}(off) = \frac{L_{gap}}{k_{air}}$

Supplementary Note 6

Constant power experiments showing only the thermal switch effect

In the battery experiments, both the battery heat generation rate and the thermal regulator's thermal conductance are changing with time, making it difficult to separate the effects from these two factors. To better isolate the effects of just the thermal regulator, in the following experiments we inserted a cartridge heater into the battery-holder assembly and used it as the heat source instead of the cells. This way, a constant heat flow (≈15W) can be provided, and the thermal switch effect can be seen more clearly.

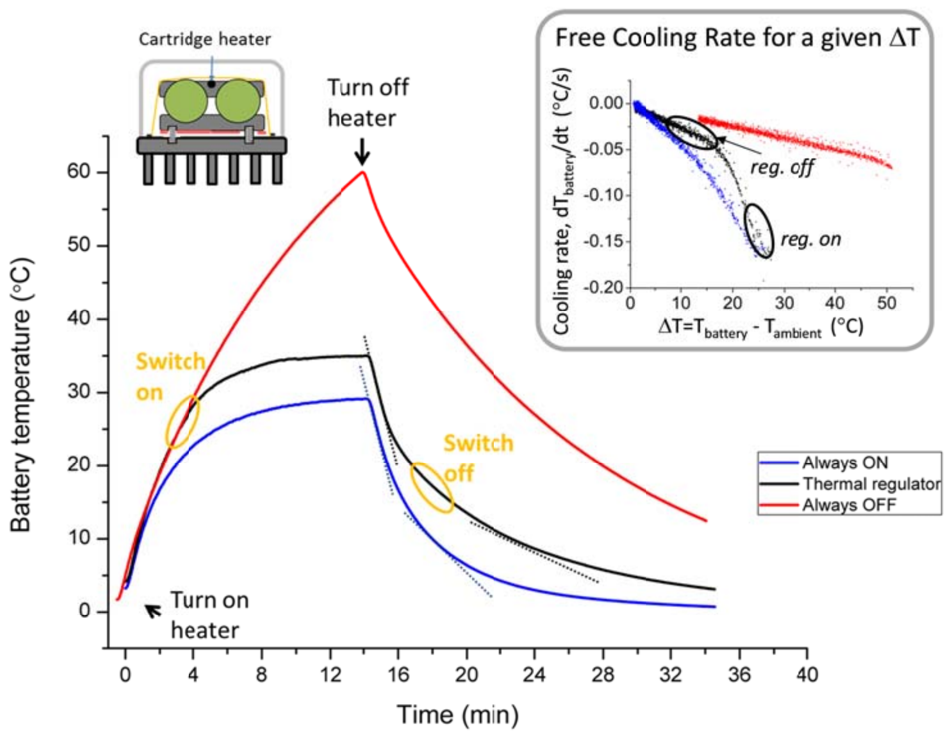

Supplementary Figure 5. Battery temperatures in response to the indicated off→on→off heating power input from the cartridge heater. Ambient temperature is T_∞=3°C in all cases. The inset shows the cooling rate obtained by numerically differentiating the data from the main panel (showing dT/dt, thus negative) vs. the driving $\Delta T = T_{battery} - T_{ambient}$. For a given ΔT, faster cooling rate indicates higher thermal conductance.

The test assembly including the fan is the same as in previous experiments except for the additional cartridge heater. Ambient temperature is 3°C. The batteries are left at open circuit throughout this experiment and all the heating come from the cartridge heater. At t=0, the heater is turned on with constant power until turned off again at roughly t=14 mins. The battery temperature is recorded for all three cases: thermal regulator, "Always ON" and "Always OFF". During the heating, the battery temperature with thermal regulator initially follows that of Always OFF, but deviates at around 30°C due to the switch effect and is capped at below 35°C, which is close to the transition completion temperature of this SMA. Then, during the free cooling process (t>14 mins), the cooling rate is an indicator of the thermal conductance. Therefore, the switch effect can be seen by comparing the three slopes at the same temperature. For example, at $T_{battery} \approx 25$°C, the "thermal regulator" slope is close to that of Always ON, but gradually approaches that of Always OFF for $T_{battery}$ below 20°C, indicating a switch-off process. To illustrate this switching-off process more clearly, the inset figure further quantifies the cooling rate continuously and shows how the thermal regulator switched from ON to OFF.

Supplementary Note 7

Thermal regulator effectiveness under abuse conditions

We tested the effectiveness of the thermal regulator under two abuse conditions: 5C rate and short circuit.

The battery module with thermal regulator is first tested for a very high 5C discharge rate in a hot environment of 45°C. The battery temperature curve is shown below in Supplementary Figure 6. High C-rate leads to high heat generation, raising the battery temperature to 67°C by the end of the discharge (module drops below the cut-off value of 5V, consistent with the main text). Some rapid temperature rise is expected for such a high C-rate, but the thermal regulator limited it to a tolerable level, successfully preventing the battery from thermal runaway. Further, as soon as the discharge finished the battery temperature quickly dropped back down, indicating that the thermal regulator maintained its conductive state.

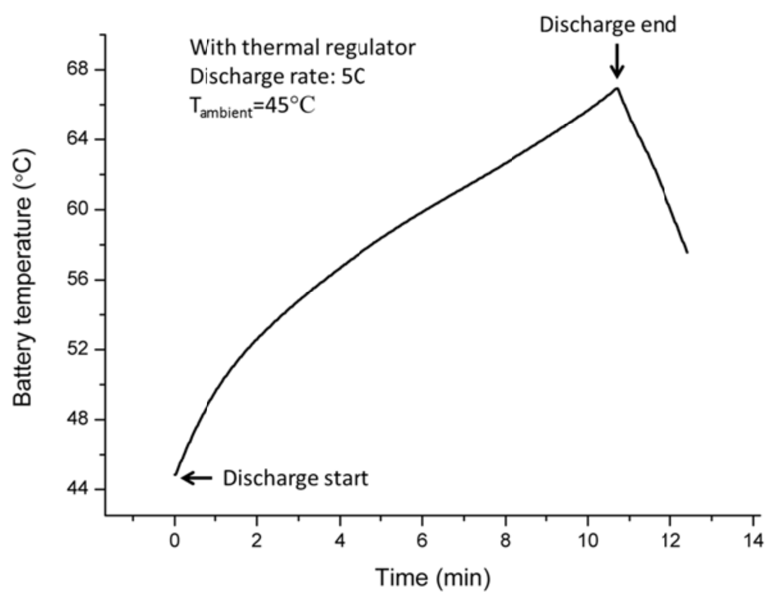

Supplementary Figure 6. Temperature response of battery module with thermal regulator discharged at 5C rate in a 45°C environment. Temperature is measured at the surface of the batteries.

To further push the limits of the battery and the device, we also executed experiments where the cells are short circuited at room temperature (the short circuit is manually stopped when cell surface temperature exceeds 65°C). Two cases, thermal regulator and "Always ON" are tested. This test does irreversible damage to the cells, and after testing these two cases the cells become completely unusable (open-circuit voltage 1.8V for the module). The battery temperature during short circuit and cooling are shown in Supplementary Figure 7. Due to the damage to the cells from the first short circuit test (we tested thermal regulator case first) we were unable to reproduce the exact heating curve for the "Always ON" case. However, the effectiveness of the thermal regulator can be seen by comparing the cooling processes for the two cases. Both cases produced nearly identical temperature curves during cooling, indicating that the thermal regulator remained ON and thermally conducting throughout the process despite the very harsh condition.

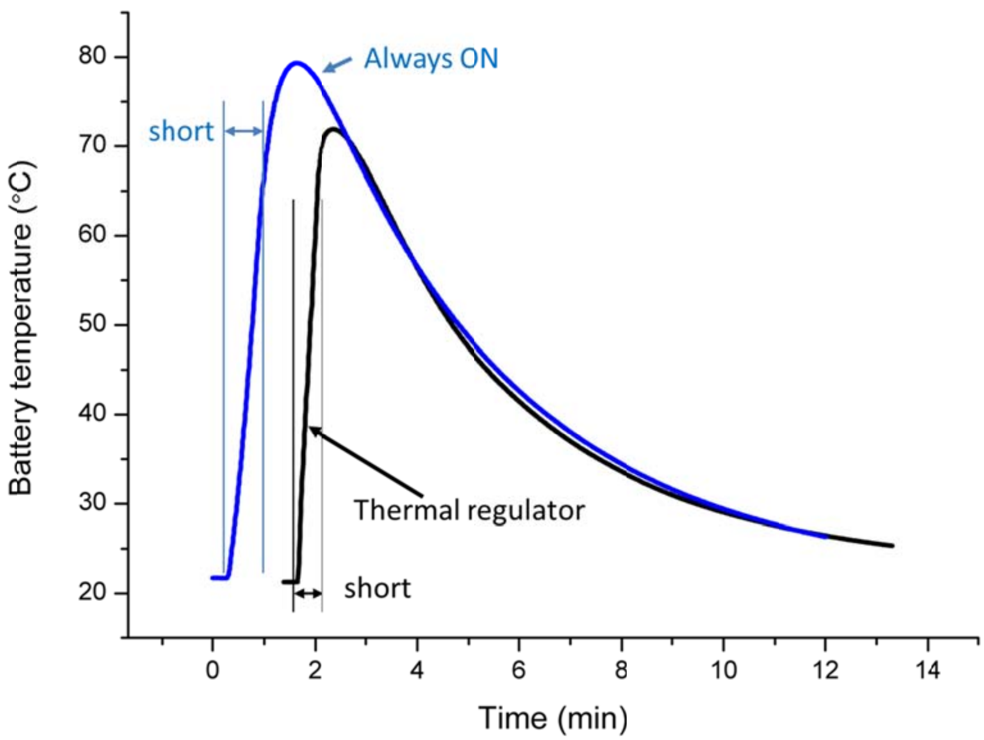

Supplementary Figure 7. Temperature response of battery module during the short circuit and the following cooling. Tests are performed at room temperature. Two cases, i.e. thermal regulator and "Always ON" are examined. Temperature is measured at the surface of the batteries. Curves are shifted along the time axis to compare the cooling parts.

Supplementary Note 8

Thermal regulator with other cells and larger packs

To study the effect of battery capacity on the effectiveness of the thermal regulator device, we also conducted experiments using the state-of-the-art 18650B NCR cells (3,500 mAh, hereafter noted as "high-cap cell") as shown below in Supplementary Figure 8. The 18650PF model ("low-cap cell", 2,700 mAh) used in the main study is stable and relatively well-understood, and was recommend by our industrial partner for fundamental research, despite having a lower capacity than the state-of-the-art cells. For a cell with a higher energy density, the heat generation rate will also be higher, assuming the same efficiency at a given C-rate. This will further improve the device's low-temperature performance (higher and more rapid temperature rise above the ambient), but make the high-temperature condition more challenging. In the case of $T_{ambient}$=-20°C, the observed lower usable relative capacity of the high-cap cell despite higher final battery temperature is a result of its poorer low-temperature characteristics, which is consistent with the datasheets [10].

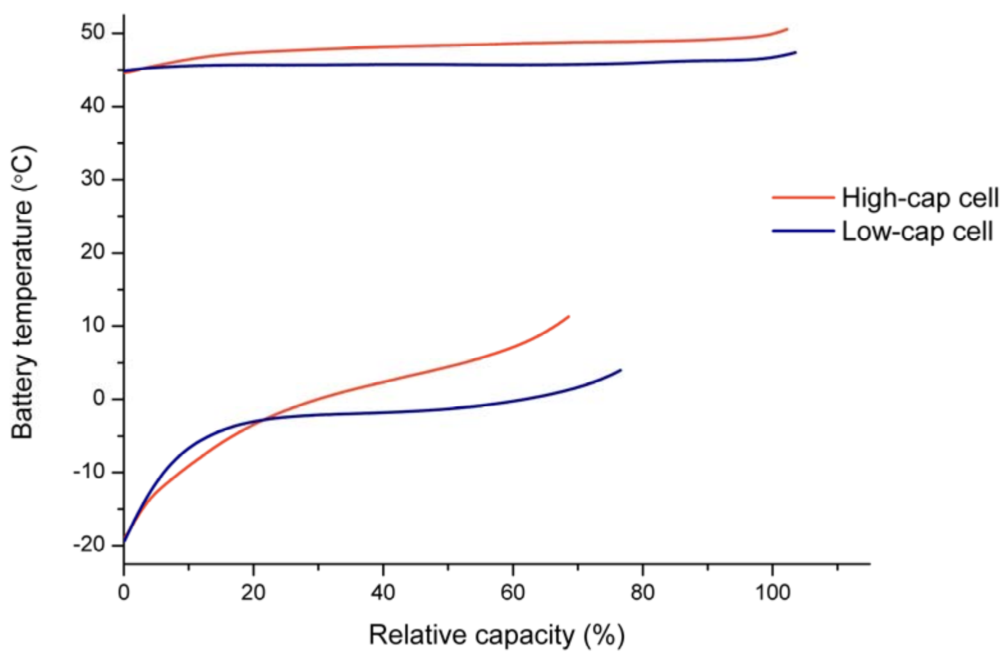

Supplementary Figure 8. Comparison of the two cell types at extreme temperatures with the same thermal regulator device. Discharge rate is 1C.

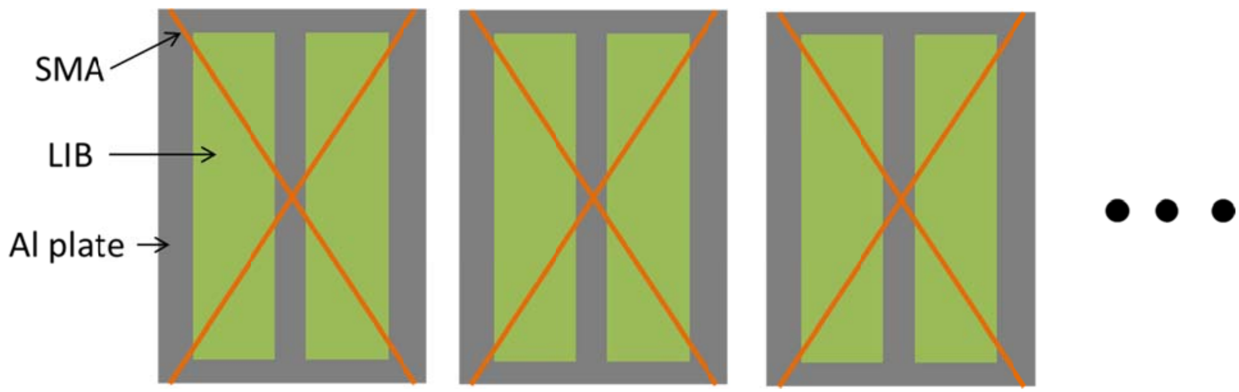

Supplementary Figure 9. Scaling up configuration #1 (top view): repetition of the modular 2-cell unit. The test module has a modular design. One solution for scaling to larger packs is to simply repeat the test unit. One advantage of this approach is that each unit's temperature is regulated individually, potentially reducing the temperature non-uniformity in a battery pack, which is currently a challenging issue for large battery packs [11].

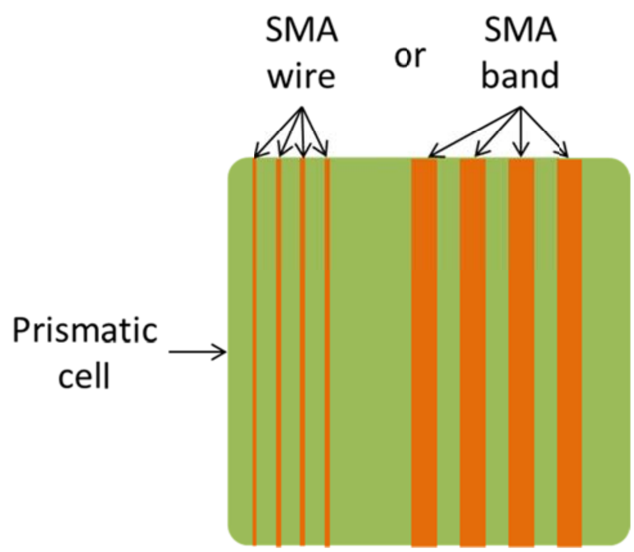

Supplementary Figure 10. Scaling up configuration #2 (top view): using SMA bands for larger individual prismatic or pouch cells. For battery packs consisting of prismatic or pouch cells, such as that of Chevy Volt or Nissan Leaf, which have larger individual weight, the number density of SMA wires should be increased accordingly. Or better yet, use SMA bands instead of wires to simplify installation and reduce stress concentration. The holder plate under the cells (gray rectangles in Supplementary Figure 7; seen also in Fig. 4a) is omitted here because it may be unnecessary since these cells already have flat surfaces.

Supplementary References

1. Prasher, R., *Thermal interface materials: historical perspective, status, and future directions.* Proceedings of the IEEE, 2006. **94**(8): p. 1571-1586.
2. Strnadel, B., et al., *Cyclic stress-strain characteristics of Ti ・ Ni and Ti ・ Ni ・ Cu shape memory alloys.* Materials Science and Engineering: A, 1995. **202**(1-2): p. 148-156.
3. Sweet, J., E. Roth, and M. Moss, *Thermal conductivity of Inconel 718 and 304 stainless steel.* International journal of thermophysics, 1987. **8**(5): p. 593-606.
4. Hao, M., K.R. Saviers, and T.S. Fisher, *Design and Validation of a High-Temperature Thermal Interface Resistance Measurement System.* Journal of Thermal Science and Engineering Applications, 2016. **8**(3): p. 031008.
5. Hartl, D.J. and D.C. Lagoudas, *Aerospace applications of shape memory alloys.* Proceedings of the Institution of Mechanical Engineers, Part G: Journal of Aerospace Engineering, 2007. **221**(4): p. 535-552.
6. Bo, Z. and D.C. Lagoudas, *Thermomechanical modeling of polycrystalline SMAs under cyclic loading, Part III: evolution of plastic strains and two-way shape memory effect.* International Journal of Engineering Science, 1999. **37**(9): p. 1175-1203.
7. *https://www.aerogel.com/products-and-solutions/cryogel-z/*.
8. *https://acc-silicones.com/products/greases/thermally-conductive-silicone-grease*.
9. Jain, A. and K.E. Goodson, *Measurement of the thermal conductivity and heat capacity of freestanding shape memory thin films using the 3ω method.* Journal of Heat Transfer, 2008. **130**(10): p. 102402.
10. *https://industrial.panasonic.com/ww/products/batteries/secondary-batteries/lithium-ion/cylindrical-type*.
11. Pesaran, A.A., *Battery thermal management in EV and HEVs: issues and solutions.* Battery Man, 2001. **43**(5): p. 34-49.